Quantum optimal control theory applied to transitions in diatomic molecules

Marius Lysebo

Department of Civil Engineering and Energy Technology, Oslo and Akershus University College of Applied Sciences, 0130 Oslo, Norway

Leif Veseth

Department of Physics, University of Oslo, 0316 Oslo, Norway

Quantum optimal control theory is applied to control electric dipole transitions in a real multilevel system. The specific system studied in the present work is comprised of a multitude of hyperfine levels in the electronic ground state of the OH molecule. Spectroscopic constants are used to obtain accurate energy eigenstates and electric dipole matrix elements. The goal is to calculate the optimal time-dependent electric field that yields a maximum of the transition probability for a specified initial and final state. A further important objective was to study the detailed quantum processes that take place during such a prescribed transition in a multilevel system. Two specific transitions are studied in detail. The computed optimal electric fields as well as the paths taken through the multitude of levels reveal quite interesting quantum phenomena.

I. INTRODUCTION

In recent years, there has been considerable progress towards the longstanding goal of controlling quantum systems using laser fields. There is currently an increasing interest in questions concerning the relation between quantum physics and information theory. Quantum logic gates could be realized by femtosecond laser pulses, and implementations on physical systems have been addressed by several authors [1–4].

Cleverly designed experiments, utilizing femtosecond laser pulses and pulse-shaping techniques, have also made it possible to control complex chemical reactions [5–9]. The automated iteration loop is a widely used experimental technique to construct optimal laser pulses. The yield of the reaction product is monitored, and the pulse is adjusted and shaped to maximize the yield.

The present work has its focus on the related theoretical methods, in particular, optimal control theory applied to quantum systems. The present work is very much based on the paper presented by Werschnik and Gross [10].

The rapidly converging iteration scheme [11–13] is adopted to be applied to diatomic molecules. The objective is to calculate laser pulses that maximize the transition probability of selected transitions. There seem to be few theoretical studies that apply control theory to diatomic molecules. Zhu *et al.* [11] calculated optimal electric fields for transitions between vibrational levels. However, this study was limited to only the vibrational levels, leaving out the fine and hyperfine structure. The reader may well ask whether the detailed molecular structure matters. Our results suggest that it does. The obtained laser pulses and the transition probabilities depend on the dipole matrix elements, which in turn depend on the fine and hyperfine structure.

The challenges involved in numerical calculations of this kind are, however, quite intractable: the number of states is large, the computational cost per iteration is significant, and the number of iterations needed to obtain a converged solution is large compared to systems with few states and well-separated energy levels.

The molecule that we have chosen to investigate is the OH molecule. It has a complex structure due to Λ doubling and hyperfine structure. With only one nuclear spin, the description of the hyperfine structure is simplified. In the present work, we present optimal electric fields for a couple of transitions between specified hyperfine states.

II. THEORY

The objective is to obtain an electric field $\varepsilon(t)$ that drives the molecular system from the initial state $|\phi_i\rangle$ to the final state $|\phi_f\rangle$. The duration of the pulse is denoted T and is one of the user-specified input parameters. It should be long enough to capture the physical processes that transform the system from the initial to the final state.

The functional to maximize takes the form [10]

$$J = J_1 + J_2 + J_3 = |\langle\phi_f|\Psi(T)\rangle|^2 - \alpha \int_0^T \varepsilon(t)^2 dt$$
$$- 2\mathrm{Im} \int_0^T \langle\chi(t)|i\frac{\partial}{\partial t} - \hat{H}|\Psi(t)\rangle dt. \tag{1}$$

The first term J_1 represents the transition probability. The second term J_2 is included to minimize the power of the electric field. A special penalty factor α is introduced to control the weight of the second term relative to the others. The optimal value of α must be obtained through trial and error. The third term J_3 requires $|\Psi(t)\rangle$ and the Lagrange multiplier $|\chi(t)\rangle$ to satisfy the Schrödinger equation.

From Eq. (1), a set of three coupled nonlinear equations in $\varepsilon(t)$, $|\Psi(t)\rangle$, and $|\chi(t)\rangle$ can be derived [10,11],

$$\alpha\varepsilon(t) = -\mathrm{Im}\langle\chi(t)|\hat{d}|\Psi(t)\rangle, \tag{2}$$

$$\hat{H}|\Psi(t)\rangle = i\frac{\partial|\Psi(t)\rangle}{\partial t}, \quad |\Psi(0)\rangle = |\phi_i\rangle, \tag{3}$$

$$\hat{H}|\chi(t)\rangle = i\frac{\partial|\chi(t)\rangle}{\partial t}, \quad |\chi(T)\rangle = |\phi_f\rangle\langle\phi_f|\Psi(T)\rangle. \tag{4}$$

The Hamiltonian in Eqs. (3) and (4) is formally written as

$$\hat{H} = \hat{H}_0 + \hat{H}_1, \tag{5}$$

where $\hat{H}_0$ [see Eq. (35)] represents the Hamiltonian for an isolated diatomic molecule, and

$$H_1 = -\vec{d} \cdot \vec{\varepsilon}(t) \qquad (6)$$

represents the interaction with an external field. In Eq. (6), $\vec{d}$ is the electric dipole moment $\vec{d} = \sum_i q_i \vec{r}_i$. (See also Sec. IV.)

A. Numerical algorithm

Equations (2)–(4) are solved using an iterative scheme, and the iteration process is summarized below.

An initial field $\varepsilon_0(t)$ is guessed to initiate the iteration process. In the present work, dc fields $\varepsilon_0(t) = \varepsilon_0$ were used. This was sufficient to obtain converged solutions. To test whether different initial electric fields were likely to result in different final electric fields, we tried an initial electric field of the form [14]

$$\varepsilon_0(t) = \varepsilon_0 \exp[-\alpha(t - T/2)^2] \cos(\omega t). \qquad (7)$$

In Eq. (7), ω represents the resonance frequency corresponding to a typical direct transition. For our test case (example A in Sec. VI A with $T = 8000$ a.u.), the final electric field did not depend on the initial electric field. However, with the initial field in Eq. (7), the number of iterations needed decreased by 1.3% compared to the dc field.

Step 0 of the algorithm is summarized below.

(1) The initial electric field $\varepsilon_0(t)$ is guessed.

(2) $|\Psi_0(0)\rangle = |\phi_i\rangle$.

(3) For all time steps t_i ($t_i = 0, \Delta t, 2\Delta t, \ldots, T - \Delta t$):

$$|\Psi_0(t_i + \Delta t)\rangle = e^{-i\hat{H}[\varepsilon_0(t_i)]\Delta t}|\Psi_0(t_i)\rangle. \qquad (8)$$

$\hat{H}$ depends on the electric field $\varepsilon_0(t_i)$, expressed by the notation $\hat{H}[\varepsilon_0(t_i)]$ in Eq. (8). The algorithm continues with step 1, summarized below.

(1) $|\chi_0(T)\rangle = |\phi_f\rangle\langle\phi_f|\Psi_0(T)\rangle$.

(2) For all time steps t_i ($t_i = T, T - \Delta t, T - 2\Delta t, \ldots, \Delta t$):

(2a) The electric field $\tilde{\varepsilon}_0(t_i)$ is computed as

$$\tilde{\varepsilon}_0(t_i) = -\frac{1}{\alpha}\text{Im}\langle\chi_0(t_i)|\hat{d}|\Psi_0(t_i)\rangle. \qquad (9)$$

(2b) $|\chi_0(t_i - \Delta t)\rangle$ is obtained by propagating $|\chi_0(t_i)\rangle$ *backwards* in time,

$$|\chi_0(t_i - \Delta t)\rangle = e^{i\hat{H}[\tilde{\varepsilon}_0(t_i)]\Delta t}|\chi_0(t_i)\rangle. \qquad (10)$$

(3) $|\Psi_1(0)\rangle = |\phi_i\rangle$.

(4) For all time steps t_i ($t_i = 0, \Delta t, 2\Delta t, \ldots, T - \Delta t$):

(4a) The electric field $\varepsilon_1(t_i)$ is computed as

$$\varepsilon_1(t_i) = -\frac{1}{\alpha}\text{Im}\langle\chi_0(t_i)|\hat{d}|\Psi_1(t_i)\rangle. \qquad (11)$$

(4b) $|\Psi_1(t_i + \Delta t)\rangle$ is obtained by propagating $|\Psi_1(t_i)\rangle$ *forwards* in time,

$$|\Psi_1(t_i + \Delta t)\rangle = e^{-i\hat{H}[\varepsilon_1(t_i)]\Delta t}|\Psi_1(t_i)\rangle. \qquad (12)$$

This completes step 1. All of the subsequent steps mirror step 1, and a general step $k > 0$ is presented below.

(1) $|\chi_{k-1}(T)\rangle = |\phi_f\rangle\langle\phi_f|\Psi_{k-1}(T)\rangle$.

(2) For all time steps t_i ($t_i = T, T - \Delta t, T - 2\Delta t, \ldots, \Delta t$):

(2a) The electric field $\tilde{\varepsilon}_{k-1}(t_i)$ is computed as

$$\tilde{\varepsilon}_{k-1}(t_i) = -\frac{1}{\alpha}\text{Im}\langle\chi_{k-1}(t_i)|\hat{d}|\Psi_{k-1}(t_i)\rangle. \qquad (13)$$

(2b) $|\chi_{k-1}(t_i - \Delta t)\rangle$ is obtained by propagating $|\chi_{k-1}(t_i)\rangle$ *backwards* in time,

$$|\chi_{k-1}(t_i - \Delta t)\rangle = e^{i\hat{H}[\tilde{\varepsilon}_{k-1}(t_i)]\Delta t}|\chi_{k-1}(t_i)\rangle. \qquad (14)$$

(3) $|\Psi_k(0)\rangle = |\phi_i\rangle$.

(4) For all time steps t_i ($t_i = 0, \Delta t, 2\Delta t, \ldots, T - \Delta t$):

(4a) The electric field $\varepsilon_k(t_i)$ is computed as

$$\varepsilon_k(t_i) = -\frac{1}{\alpha}\text{Im}\langle\chi_{k-1}(t_i)|\hat{d}|\Psi_k(t_i)\rangle. \qquad (15)$$

(4b) $|\Psi_k(t_i + \Delta t)\rangle$ is obtained by propagating $|\Psi_k(t_i)\rangle$ *forwards* in time,

$$|\Psi_k(t_i + \Delta t)\rangle = e^{-i\hat{H}[\varepsilon_k(t_i)]\Delta t}|\Psi_k(t_i)\rangle. \qquad (16)$$

B. Explicit form of the propagator

The formal propagator

$$e^{-i\hat{H}[\varepsilon(t)]\Delta t} = e^{-i\hat{H}_0\Delta t + i\varepsilon(t)\hat{d}\Delta t} \qquad (17)$$

is approximated by the symmetric second-order splitting scheme [15], accurate to second order in Δt. The propagators for the time steps $t \rightarrow (t + \Delta t)$ and $t \rightarrow (t - \Delta t)$ take the form

$$|\Psi(t + \Delta t)\rangle = \exp\left(-i\hat{H}_0\frac{\Delta t}{2}\right)\exp[i\hat{d}\varepsilon(t)\Delta t]$$
$$\times \exp\left(-i\hat{H}_0\frac{\Delta t}{2}\right)|\Psi(t)\rangle, \qquad (18)$$

$$|\chi(t - \Delta t)\rangle = \exp\left(i\hat{H}_0\frac{\Delta t}{2}\right)\exp[-i\hat{d}\varepsilon(t)\Delta t]$$
$$\times \exp\left(i\hat{H}_0\frac{\Delta t}{2}\right)|\chi(t)\rangle. \qquad (19)$$

The molecular state $|\Psi(t)\rangle$ [and also $|\chi(t)\rangle$] is, at any instant of time, expanded in terms of the molecular eigenstates of $\hat{H}_0$, labeled $|\psi_j\rangle$,

$$|\Psi(t)\rangle = \sum_j c_j(t)|\psi_j\rangle. \qquad (20)$$

We now make the approximation

$$e^{i\hat{d}\varepsilon(t)\Delta t} \simeq 1 + i\hat{d}\varepsilon(t)\Delta t, \qquad (21)$$

which is reasonable only for sufficiently small time steps Δt. We attempted to go beyond this approximation and include the second-order term $-\hat{d}^2\varepsilon(t)^2\frac{\Delta t^2}{2}$. This did not improve the convergence properties. It did, however, increase the number of floating point operations per iteration, and thereby the computational cost.

Obviously,

$$e^{-i\hat{H}_0\frac{\Delta t}{2}}|\psi_j\rangle = e^{-iE_j\frac{\Delta t}{2}}|\psi_j\rangle, \qquad (22)$$

and

$$\hat{d}|\psi_j\rangle = \sum_k d_{jk}|\psi_k\rangle. \qquad (23)$$

The coefficients $d_{jk} = \langle \psi_k | \hat{d} | \psi_j \rangle$. From Eqs. (18) and (21), it now follows that

$$|\Psi(t + \Delta t)\rangle \simeq e^{-i\hat{H}_0 \frac{\Delta t}{2}}[1 + i\hat{d}\varepsilon(t)\Delta t]e^{-i\hat{H}_0 \frac{\Delta t}{2}}|\Psi(t)\rangle. \quad (24)$$

In practice, the vector $|\Psi(t + \Delta t)\rangle$ is obtained by repeated multiplications $|\Psi(t + \Delta t)\rangle = A|\Psi(t)\rangle$. The coefficients A_{mn} of the matrix A are obtained from Eqs. (24), (22), and (23) and take the form

$$A_{mn} = e^{-iE_n\Delta t}\delta_{mn} + e^{-i(E_m+E_n)\frac{\Delta t}{2}}d_{mn}\varepsilon(t)\Delta t. \quad (25)$$

The vector $\Psi(t)$ has components [cf. Eq. (20)]

$$\Psi(t) = \begin{pmatrix} c_1(t) \\ c_2(t) \\ \cdots \\ c_N(t) \end{pmatrix}. \quad (26)$$

The off-diagonal elements of A depend on t and are updated for each time step, whereas the diagonal elements are independent of t. Similar expressions for $|\chi(t - \Delta t)\rangle$ are found by making the substitution $\Delta t \rightarrow -\Delta t$.

III. THE MOLECULAR BASIS STATES

The basis states are Hund's coupling case (a_β) [16,17], with a slight modification. In Hund's case (a_β), the nuclear spin angular momentum $\vec{I}$ is coupled to $\vec{J}$ to form the grand total angular momentum $\vec{F} = \vec{I} + \vec{J}$. Hence, $\vec{J}$ represents the total angular momentum *excluding* nuclear spin, and the corresponding quantum numbers are half integers for the present system. The corresponding quantum numbers for the grand total angular momentum $\vec{F}$ are integers. (See also Fig. 1.)

The Hamiltonian that represents the hyperfine interaction is most easily expressed in a basis in which the nuclear spin states are quantized along the molecular axis. The nuclear spin states are denoted $|I\Omega_I\rangle$. Hence, the molecular basis states $|\varphi\rangle$ are written

$$|\varphi\rangle = |nv\Lambda\Sigma S\rangle|I\Omega_I\rangle|FM_F\Omega_F\rangle = |nv\Lambda\Sigma SI\Omega_I FM_F\Omega_F\rangle. \quad (27)$$

In Eq. (27), v represents the vibrational quantum number; Λ, Σ, and Ω_I refer to the quantized components of the electronic orbital, the spin angular momentum, and the nuclear spin angular momentum along the molecular axis. $\vec{S}$ and $\vec{I}$ are now assumed to be quantized along the molecular axis. $\Omega_F \equiv \Lambda + \Sigma + \Omega_I$ and represents the projection of the total angular momentum along the molecular axis, whereas M_F denotes the quantized component of $\vec{F}$ along a space fixed axis. S and I denote the electronic and nuclear spin quantum numbers. Finally, n is a label introduced to distinguish between states with otherwise identical quantum numbers. S and I are merely constants for OH, with the numerical value $S = I = \frac{1}{2}$. The transformation between the molecular basis states corresponding to Hund's coupling case (a_β) and the ones in Eq. (27) is given in Eq. (B11).

The reader may well ask what happened to the quantum number J. The price we pay for quantizing the projection of the nuclear spin along the molecular axis is the quantum number J. However, the molecular eigenstates (Sec. V) will be (approximate) eigenfunctions of $\vec{J}^2$, and the energy levels

can be grouped according to the value of J, as seen in Fig. 1. Obviously, the basis states in Eq. (27) might not offer a very good first-order description of the system, but it is easy to set up the matrix elements of the Hamiltonian in this basis, and that is important.

The symmetry properties of the molecular basis states $|\varphi\rangle$ need a more in-depth discussion than we are prepared to provide in the present work. The interested reader is therefore referred to the literature [18–22]. However, the effect of the total inversion operator $\hat{E}^*$ (inversion of all coordinates) on the basis states is given by

$$\hat{E}^*|nv\Lambda\Sigma SI\Omega_I FM_F\rangle$$
$$= (-1)^{F-S-I+s_n}|nv-\Lambda-\Sigma SI-\Omega_I FM_F\rangle, \quad (28)$$

with $s_n = 0$ for all but Σ^- states where $s_n = 1$.

Eigenstates for the inversion operator E^* are obtained by forming the linear combinations

$$|\psi\rangle = \frac{1}{\sqrt{2}}(|nv\Lambda\Sigma SI\Omega_I FM_F\rangle \pm (-1)^{F-S-I+s_n}|nv-\Lambda$$
$$-\Sigma SI - \Omega_I FM_F\rangle), \quad (29)$$

with corresponding eigenvalues ± 1 obtained from the simple eigenvalue equation,

$$\hat{E}^*|\psi\rangle = \pm|\psi\rangle. \quad (30)$$

IV. THE DIPOLE OPERATOR

The electric dipole moment $\vec{d}$ is defined by $\vec{d} = \sum_i q_i \vec{r}_i$, where the sum extends over all electrons and nuclei. The Hamiltonian for a molecular system interacting with an external electric field $\vec{\varepsilon}$ takes the form

$$H_1 = -\vec{d} \cdot \vec{\varepsilon} = -\sum_{\mu=-1}^{1}(-1)^\mu d_{-\mu}\varepsilon_\mu, \quad (31)$$

where ε_μ are the spherical components of the external electric field. We now assume that the electric field has just one component, $\varepsilon_0 = \varepsilon_z$, corresponding to linearly polarized light.

The matrix elements $\langle\varphi'|\hat{d}_z|\varphi\rangle$ are most easily obtained by transforming d_z into a molecule-fixed system,

$$d_z = \sum_{m=-1}^{1} \mathcal{D}_{0m}^{(1)}(\phi,\theta,0)^* d_m. \quad (32)$$

In Eq. (32), $\mathcal{D}_{0m}^{(1)}$ represents the components of a rotation matrix [23], and d_m are the spherical components of the electric dipole operator in the molecule-fixed system. A general matrix element $\langle\varphi'|\hat{d}_z|\varphi\rangle$ then takes the form (see Appendix A or Ref. [22])

$$\langle n'v'\Lambda'\Sigma\Omega_I F'M_F|\hat{d}_z|nv\Lambda\Sigma\Omega_I FM_F\rangle$$
$$= \sum_{m=-1}^{1} \langle n'v'\Lambda'\Sigma|\hat{d}_m|nv\Lambda\Sigma\rangle \times (-1)^{M_F-\Omega'_F-m}$$
$$\times \sqrt{(2F'+1)(2F+1)} \times \begin{pmatrix} F & 1 & F' \\ \Omega_F & -m & -\Omega'_F \end{pmatrix}$$
$$\times \begin{pmatrix} F & 1 & F' \\ M_F & 0 & -M_F \end{pmatrix}, \quad (33)$$

where the addition of the angular momenta is expressed in terms of the $3j$ symbols, rather than in terms of the
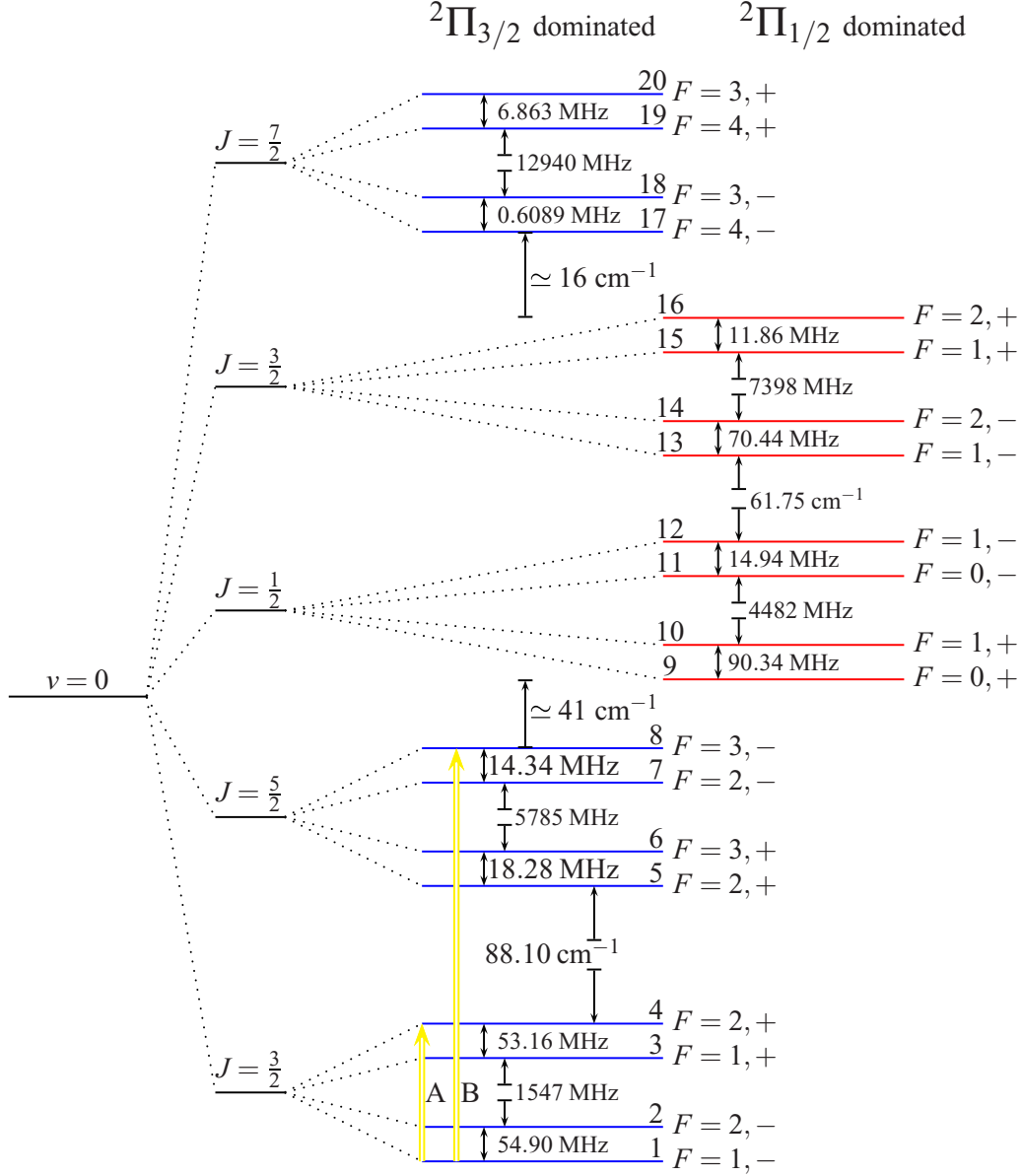
FIG. 1. (Color online) Selected energy levels with total molecular angular momentum $F = 0,1,2,3$, and 4, corresponding to $v = 0$ (not to scale). The yellow lines represent the transitions studied in examples A and B. The figure shows levels corresponding to the $^2\Pi_{3/2}$ state (blue lines) in the left column, while the (red) levels in the right column correspond to the $^2\Pi_{1/2}$ state.

Clebsch-Gordan coefficients. The projection of the total molecular angular momentum along the molecular axis has been defined in Eq. (33) as $\Omega_F \equiv \Lambda + \Sigma + \Omega_I$. The matrix elements $\langle\varphi'|\hat{d}_z|\varphi\rangle$ between states of different Σ, Ω_I, or M_F quantum numbers are zero. It also follows from the properties of the $3j$ symbols of Eq. (33) that $\langle\varphi'|\hat{d}_z|\varphi\rangle$ differs from zero only when $F' = F \pm 1$ and $\Omega'_F = \Omega_F - m$.

The matrix element of the electric dipole moment between parity eigenstates [see Eq. (29)] takes the form [24]

$$\langle\psi'|\hat{d}_z|\psi\rangle$$
$$= \tfrac{1}{2}[1 - (-1)^s]\langle v'\Lambda'\Sigma\Omega_I F'M_F|\hat{d}_z|v\Lambda\Sigma\Omega_I FM_F\rangle, \quad (34)$$

with $\Lambda \geqslant 0$ and $\Lambda' \geqslant 0$. $s = 0$ if $|\psi\rangle$ and $|\psi'\rangle$ have the same parity, and $s = 1$ if $|\psi\rangle$ and $|\psi'\rangle$ have opposite parities. In

its general form, Eq. (34) does not apply for $\Lambda = \Sigma = 0$ ($\Lambda' > 0$) or $\Lambda' = \Sigma' = 0$ ($\Lambda > 0$). However, such transitions are not considered in the present work. For the special case $\Lambda = \Lambda' = 0$, the corresponding Σ quantum numbers must be positive or zero.

Numerical values for the electric dipole elements $\langle n'v'\Lambda'|\hat{d}_m|nv\Lambda\rangle$ of Eq. (33) are obtained from Stevens *et al.* [25].

V. THE MOLECULAR EIGENSTATES

The diatomic Hamiltonian can be formally written as

$$\hat{H}_0 = \hat{H}_{ev} + \hat{H}_{\text{rot}} + \hat{H}_{hf}, \quad (35)$$

where $\hat{H}_{ev}$ denotes the electronic and vibrational Hamiltonian, $\hat{H}_{rot}$ represents the rotational energy operator, and $\hat{H}_{hf}$ represents the hyperfine operator.

The general matrix element $\langle\psi'|\hat{H}_0|\psi\rangle$ is rather involved and is not reproduced here. It can be found in the literature [26,27]. Diagonalization of this matrix gives the energy eigenstates and the energies. The energy eigenstates are characterized by the quantum numbers n, v, Λ, J, F, Ω_F, M_F, and the parity eigenvalue ± 1. In addition, $\Omega = \Lambda + \Sigma$ will in the present case be approximately a "good" quantum number after diagonalization.

A few spectroscopic parameters are needed. These are the hyperfine parameters (a, b, c, and d), the Λ-doubling parameters (p and q), and the spin-orbit interaction constant A. Numerical values for these parameters have been obtained from Beaudet and Poynter [28] for the electronic ground state ($X^2\Pi$) of OH.

The definitions of the hyperfine parameters can be found in Refs. [29–31]. The spin-orbit coupling constant as well as the Λ-doubling parameters are defined and described by Coxon and Foster [32].

The internuclear potential curve is modeled as a Morse potential. The internuclear potential curve is only used to obtain the rotational constants B_v, by averaging $\frac{1}{2\mu R^2}$ over the vibrational wave functions. R represents the internuclear distance.

VI. NUMERICAL EXAMPLES

In this section, we consider transitions between energy eigenstates of definite parity. The initial state is labeled $|\phi_i\rangle$ and the final state is labeled $|\phi_f\rangle$. The objective is to obtain an electric field $\varepsilon(t)$ that maximizes the transition probability $P = |\langle\phi_f|\Psi(T)\rangle|^2$.

The convergence criteria employed throughout the present work are

$$\eta_1 = \frac{|P_{new} - P_{old}|}{|P_{new}|} < 10^{-6}, \quad \eta_2 = \frac{|J_{2,new} - J_{2,old}|}{|J_{2,new}|} < 10^{-6}, \tag{36}$$

where P represents the transition probability and J_2 was defined in Eq. (1). The terms "new" and "old" refer to the present and past iteration cycles. Both criteria in Eq. (36) must be met before the iterations are terminated.

The electric dipole transitions are subject to the following selection rules: $\Delta J = 0, \pm 1, + \leftrightarrow -$ (parity) and $\Delta F = 0, \pm 1$. $\Omega = \Lambda + \Sigma$ is only approximately a good quantum number, hence there are nonzero transition moments between states with different Ω values.

Even when the dipole matrix element $\langle\phi_f|\hat{d}|\phi_i\rangle$ is small or zero, electric fields that yield considerable transition probabilities can be obtained. This is possible through sequences of transitions between intermediate states connecting $|\phi_i\rangle$ and $|\phi_f\rangle$. In these cases, the population is transferred from $|\phi_i\rangle$ to $|\phi_f\rangle$ via intermediate states with large (or at least larger) electric dipole moments "bridging the gap" between the initial and the final state. These transitions are only possible when the duration of the pulse T is long enough to allow for the physical processes.

TABLE I. Dipole matrix elements for transitions from state $|1\rangle$ to states of opposite parity. j refers to the labels introduced in Fig. 1. The matrix elements $\langle 3|\hat{d}|1\rangle$, $\langle 10|\hat{d}|1\rangle$, and $\langle 15|\hat{d}|1\rangle$ are zero due to the second $3j$ symbol in Eq. (33).

j	$\langle j|\hat{d}|1\rangle$ (a.u.)	j	$\langle j|\hat{d}|1\rangle$ (a.u.)
3	0.00	10	0.00
4	0.13	15	0.00
5	−0.27	16	−0.015
9	−0.055		

The ground electronic state of OH ($X^2\Pi$) has a rather complex structure due to Λ doubling and the magnetic hyperfine interaction. A selection of energy levels for the electronic and vibrational ground state is shown in Fig. 1. In the numerical calculations, a total of 56 states are included to obtain the molecular energy eigenstates and dipole matrix elements.

A. Transition within a Λ doublet with hyperfine splitting

As a concrete example, we consider a transition between hyperfine states in the lowest electronic and vibrational state:

$$\begin{aligned} |\phi_i\rangle = |1\rangle &= |X^2\Pi_{3/2}(v = 0), \\ J = 3/2, F &= 1, M_F = 0, -\rangle \rightarrow \\ |\phi_f\rangle = |4\rangle &= |X^2\Pi_{3/2}(v = 0), \\ J = 3/2, F &= 2, M_F = 0, +\rangle. \end{aligned} \tag{37}$$

The initial state is the ground state. The final state differs from the initial state by the total molecular angular momentum F and the parity. The labels 1 and 4 in Eq. (37) refer to Fig. 1. The energy difference between the hyperfine states $|1\rangle$ and $|4\rangle$ is approximately 1655 MHz.

Table I presents the electric dipole moments $\langle j|\hat{d}|1\rangle$ for the dipole allowed transitions ($\Delta F = 0, \pm 1, + \leftrightarrow -$) between the initial state $|1\rangle$ and the states included in Fig. 1. The final state $|4\rangle$ was originally chosen because of the favorable dipole matrix element $\langle 4|\hat{d}|1\rangle$. The intention was then to present a simple and direct transition as a first example. However, as the present work evolved, the results were surprisingly rich, and the transition $|1\rangle \rightarrow |4\rangle$ proved to be neither simple nor direct.

Additional dipole matrix elements will turn out to be relevant for the present example. The magnitude of the electric dipole moments $|\langle j|\hat{d}|i\rangle|$ between all of the 20 states included in Fig. 1 are compared in Fig. 2. The states that couple to $|\phi_i\rangle = |1\rangle$ or $|\phi_f\rangle = |4\rangle$ are of particular interest. They are easily identified from Fig. 2.

The dipole moments depend on the detailed inner structure of the molecule, and their values obviously have significant influences on the final results. A large number of molecular basis states (see Sec. III) must be included in the calculation to obtain reliable molecular energy eigenstates and transition dipole moments. The computational cost needed to diagonalize the Hamiltonian [Eq. (35)] in this basis is rather modest and does not present any problem.
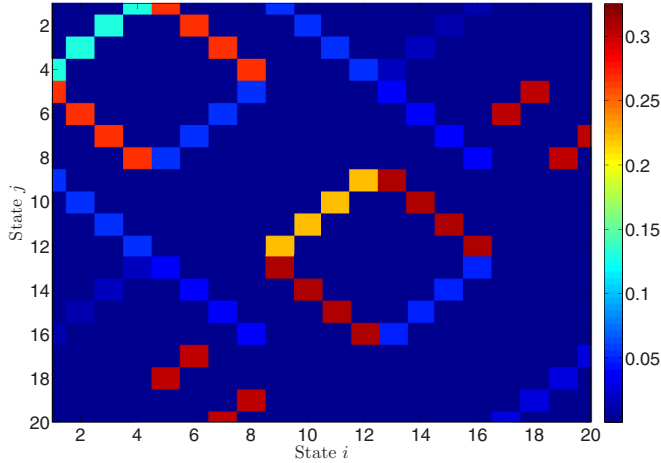
FIG. 2. (Color online) Absolute value of electric dipole moments $|\langle j|\hat{d}|i\rangle|$ for the states drawn in Fig. 1. In example A, the initial state is $|1\rangle$ and the final state is $|4\rangle$.

Once energy eigenstates and dipole matrix elements have been calculated, the iteration process leading to an optimized electric field is initiated. At this point, it may be tempting to treat the molecule as a simple two-level system (see Fig. 1). After all, both states $|2\rangle$ and $|3\rangle$ are unaccessible from $|1\rangle$. However, such restrictions have a profound influence on the obtained solution to the control equations. Compared to a realistic multilevel calculation, the number of iterations needed to obtain a converged solution drops to well below 100, and

the transition probability increases to 1.0. Such results are, of course, unreliable and invalid because the two-level model is too simple to describe the physical processes. Clearly we need to determine the number of states to include in the iteration scheme. The dipole moments provide a guidance. States that do not couple to the initial or final state, i.e., that are completely unaccessible, can be ignored at this stage. Obviously, additional restrictions must be implemented as well, otherwise the computational cost would be unbearable. We have not included excited vibrational states, or states with corresponding quantum number $F > 7$. This represents a source of uncertainty, minimized by trial and error, but never eliminated.

The transition probabilities $|\langle 4|\Psi(T)\rangle|^2$ as a function of the number of iterations are shown in the upper panel of Fig. 3 for pulses of different length T.

When $T = 20\,000$ a.u., the convergence criteria [Eq. (36)] are met after approximately $40\,000$ iterations, and the transition probability is 1.0 (solid blue line). However, the final transition probability depends on the duration of the pulse T. A few examples with $T = 10\,000, 8000$, and 6000 a.u. are included in Fig. 3, whereas Fig. 4 presents the final transition probability as a function of T.

The transition probability $|\langle 4|\Psi(T)\rangle|^2$ increases rapidly from 0.15 at $T = 4000$ a.u. to 0.50 at $T = 5000$ a.u. At $T > 15\,000$ a.u., the transition probability is close to 1.0, but oscillates as a function of T. The origin of these oscillations is not known. The oscillations do not depend on the time step Δt, therefore we do not believe that they can be explained simply as the sign of increasing truncation errors.
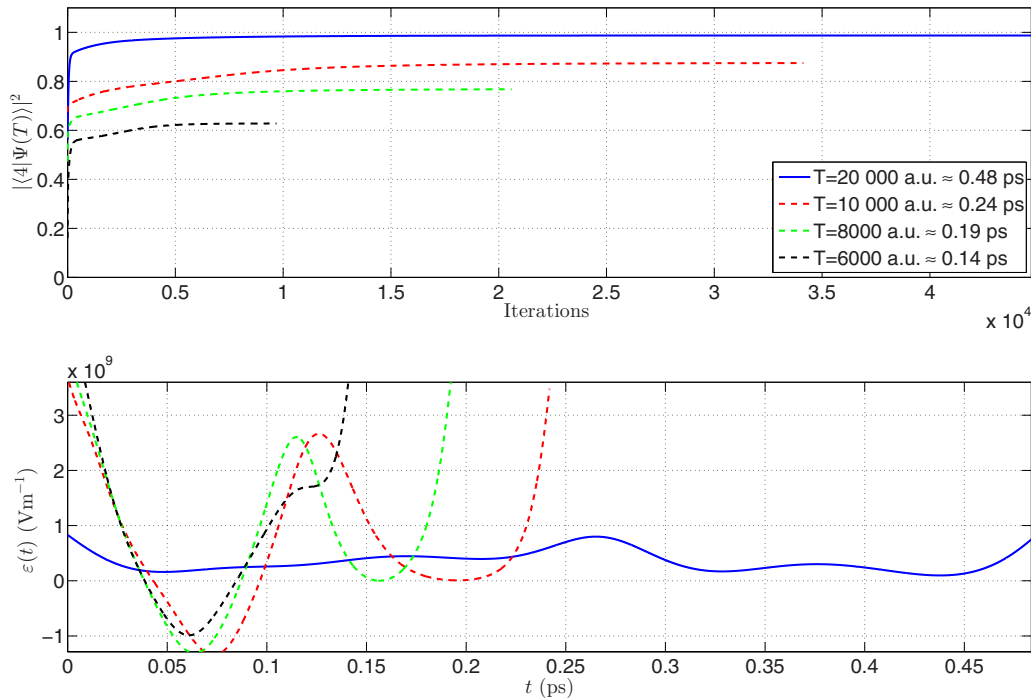

FIG. 3. (Color online) Upper panel: Transition probability as a function of iterations for the transition $|1\rangle \rightarrow |4\rangle$ (see Fig. 1). The dashed lines show the transition probabilities for optimal pulses of different durations (see the legend). The lines terminate at the number of iterations where the criteria of Eq. (36) are fulfilled. Lower panel: Optimized electric field $\varepsilon(t)$ obtained for pulses of different durations T. The number of iterations needed for a convergent solution vary with T, as seen in the upper panel. Key parameters: $\Delta t = 0.005$, $\epsilon_0 = 0.001$, $\alpha = 1$, all expressed in atomic units.
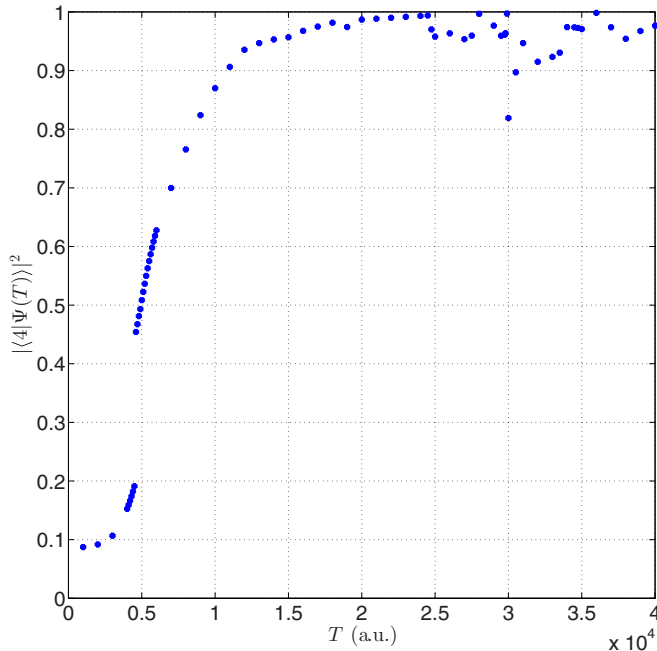
FIG. 4. (Color online) Transition probability $|\langle 4|\Psi(T)\rangle|^2$ as a function of the duration of the pulse T. Electric fields of duration $T < 4000$ a.u. do not yield significant transition probabilities.

A rapid increase in the transition probability between $T = 4000$ a.u. and $T = 5000$ a.u. is seen in Fig. 4. At $T = 5000$ a.u., the algorithm converges to a different solution compared to the solution obtained at 4000 a.u. It should be noted that Demiralp and Rabitz [33] have previously shown that there are multiple solutions to quantum control problems. The precise value of T where this "crossover" between solutions occurs depends slightly on the guessed initial field ε_0.

The number of iterations needed to reach a convergent solution depends on the duration of the pulse T, the penalty factor α, and the (guessed) initial electric field ε_0. Numerical experiments suggest that the relationship between the number of iterations needed to obtain a convergent solution and the duration of the pulse T is complicated. There is a rapid increase in the number of iterations until $T = 13\,000$ a.u. For $T > 15\,000$ a.u., the number actually varies from 2700 to 24\,000. In these numerical experiments, the guessed initial electric field ε_0 was unchanged.

The lower panel of Fig. 3 shows the optimized electric fields $\varepsilon(t)$ as a function of time for pulses of different length T. The amplitudes of the field oscillations are seen to increase when T decreases, and for the short pulses the transition probability does not reach unity. However, for the present example, the optimal electric fields appear to be of primarily theoretical interest and do not seem to be well suited for experiments. No restrictions have been imposed on the obtained optimal fields.

Figure 5 shows occupation probabilities of selected states as a function of time $t \in [0, T]$ for two optimized electric fields of different duration T. The selected states are the ones that achieve an occupation probability larger than 0.05 with the optimized electric field.

In addition to the initial state $|1\rangle$ (solid blue line) and the final state $|4\rangle$ (solid red line), other states are found to have

significant occupation probabilities during the time $t \in [0, T]$ as well. State $|5\rangle$ (red dashed line) is readily accessible from the initial state due to the large dipole matrix element connecting the two states. (See also Table I and Fig. 2.) However, the final state and state $|5\rangle$ have the same parity. An intermediate state is therefore needed to reach the final state from state $|5\rangle$. This is identified as state $|8\rangle$ with the corresponding occupation probability represented as a dashed blue line in Fig. 5.

With the optimized electric field for the duration $T = 10\,000$ a.u., state $|18\rangle$ attains a significant occupation probability. This state is populated from state $|5\rangle$, as seen in the lower panel of Fig. 5. With reference to Fig. 1, this may appear somewhat surprising. However, Fig. 2 clearly shows a strong coupling between $|5\rangle$ and $|18\rangle$. Still, it is rather remarkable that the system takes a detour to such a highly excited state on its way to $|4\rangle$.

The occupation probabilities presented in Fig. 5 are very different from simple two-level systems with their well-known Rabi oscillations. In particular, the occupation probabilities have a much more complicated dependence on the duration of the pulse T. As T is extended, the intermediate occupation probabilities change completely because the electric field is redesigned for every T (cf. Fig. 3).

From the preceding discussion, some important pathways between the initial and final states are identified:

$$|1\rangle \rightarrow |4\rangle, \tag{38}$$

$$|1\rangle \rightarrow |5\rangle \rightarrow |4\rangle, \tag{39}$$

$$|1\rangle \rightarrow |5\rangle \rightarrow |8\rangle \rightarrow |4\rangle, \tag{40}$$

$$|1\rangle \rightarrow |5\rangle \rightarrow |18\rangle \rightarrow |5\rangle \rightarrow |4\rangle. \tag{41}$$

The path chosen by the system clearly depends on the duration of the pulse T, as shown for $T = 10\,000$ and $T = 20\,000$ a.u. in Fig. 5. Based on the results presented in Fig. 5, it may seem natural to assume that the complexities of the pathways chosen by the systems decrease with increasing T. However, additional numerical experiments with $T > 20\,000$ a.u. do not support this conclusion. In fact, the results suggest that an increase in T may lead to even more complicated paths, including additional intermediate states. This observation might indicate that there is an "optimal" duration time T for which the transition passes in a smooth and adiabatic manner.

The objective functional to be optimized in this case (neglecting J_3) is

$$J = J_1 + J_2 = |\langle 4|\Psi(T)\rangle|^2 - \alpha \int_0^T \varepsilon(t)^2 dt. \tag{42}$$

Figure 6 shows J_2 as a function of the number of iterations for fields of duration $T = 20\,000, 10\,000, 8000,$ and 6000 a.u. J_1 adds the main contribution to the sum in Eq. (42) in this case. The occupation probability J_1 at the final time T is above 0.5 in all cases, whereas $|J_2| < 0.08$ for all T values. The relative weight of J_2 is controlled by the parameter α, which in the present case was set equal to unity.

From Figs. 3 and 6, we conclude that the electric field needs to be more powerful when the duration of the pulse is decreased. It is not surprising to find that more power is
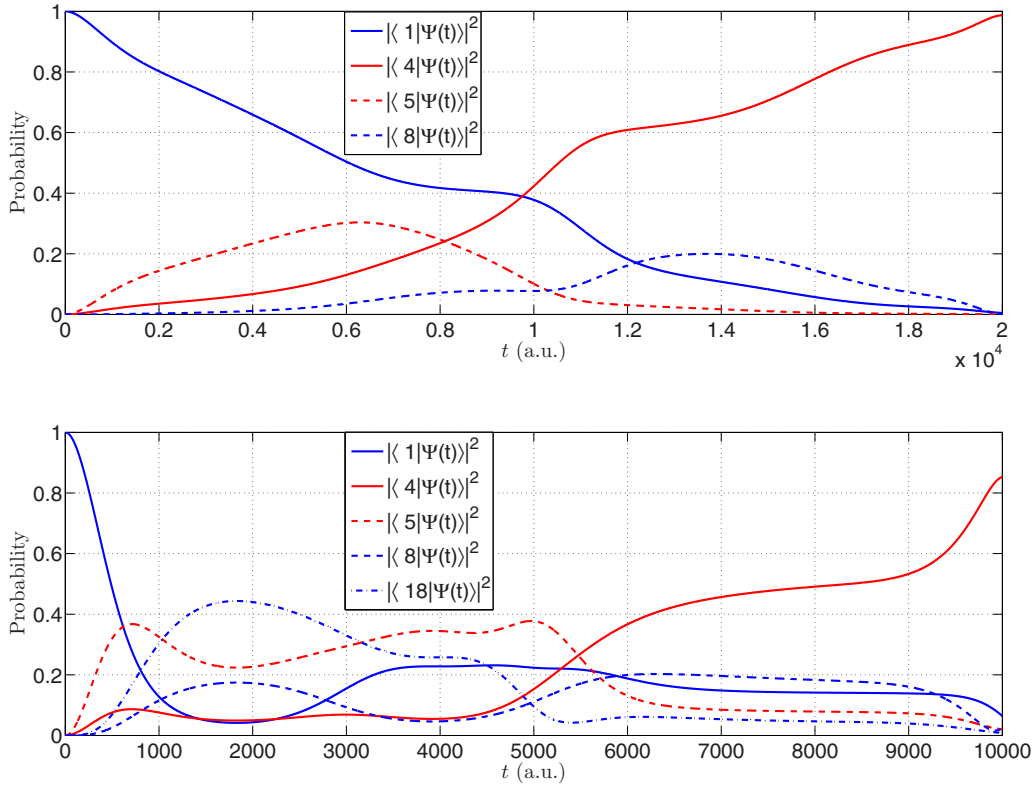
FIG. 5. (Color online) Occupation probabilities as a function of time for the initial and final states (solid lines), together with the intermediate states (dashed lines). Red (blue) is used to identify states with parity eigenvalue $+1$ (-1). Upper panel: Occupation probabilities obtained with the optimized electric field of duration $T = 20\,000$ a.u. $\simeq 0.48$ ps. Lower panel: Occupation probabilities obtained with the optimized electric filed of duration $T = 10\,000$ a.u. $\simeq 0.24$ ps.

necessary to transfer the population in a shorter time frame. The difference between $T = 10\,000$ a.u. and $T = 20\,000$ a.u. is, however, quite prominent, and once again we can only emphasize the importance of the duration T. Throughout the present paper, it is repeatedly documented that the value of T has an important impact on all other results.
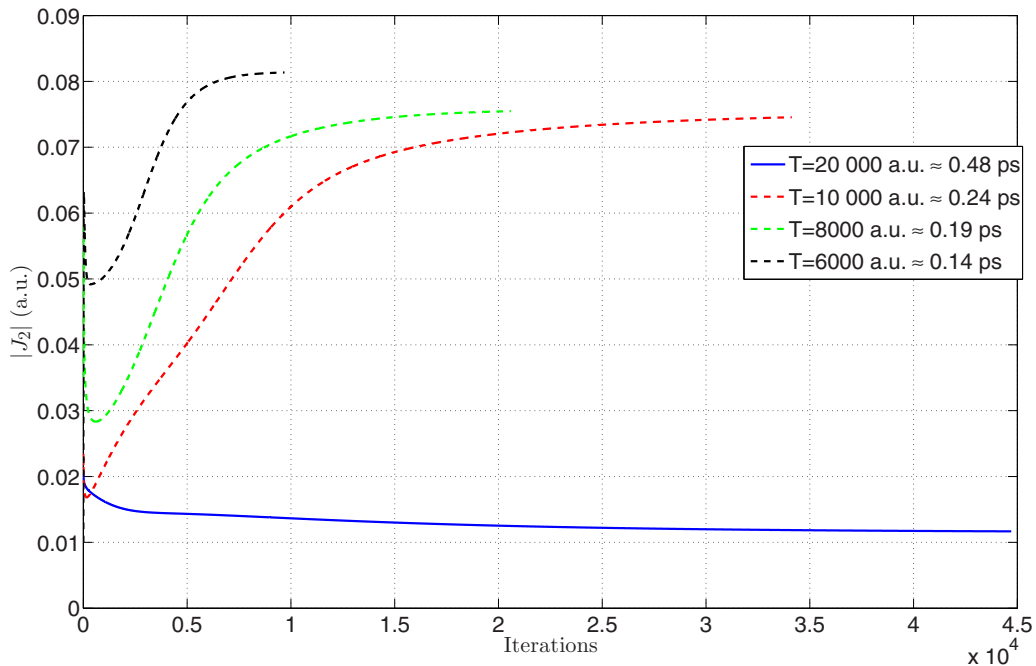

FIG. 6. (Color online) The quantity $|J_2|$ [see Eq. (42)] as a function of the number of iterations for example A. The iterations for the various values of T are terminated when the criteria of Eq. (36) are fulfilled.
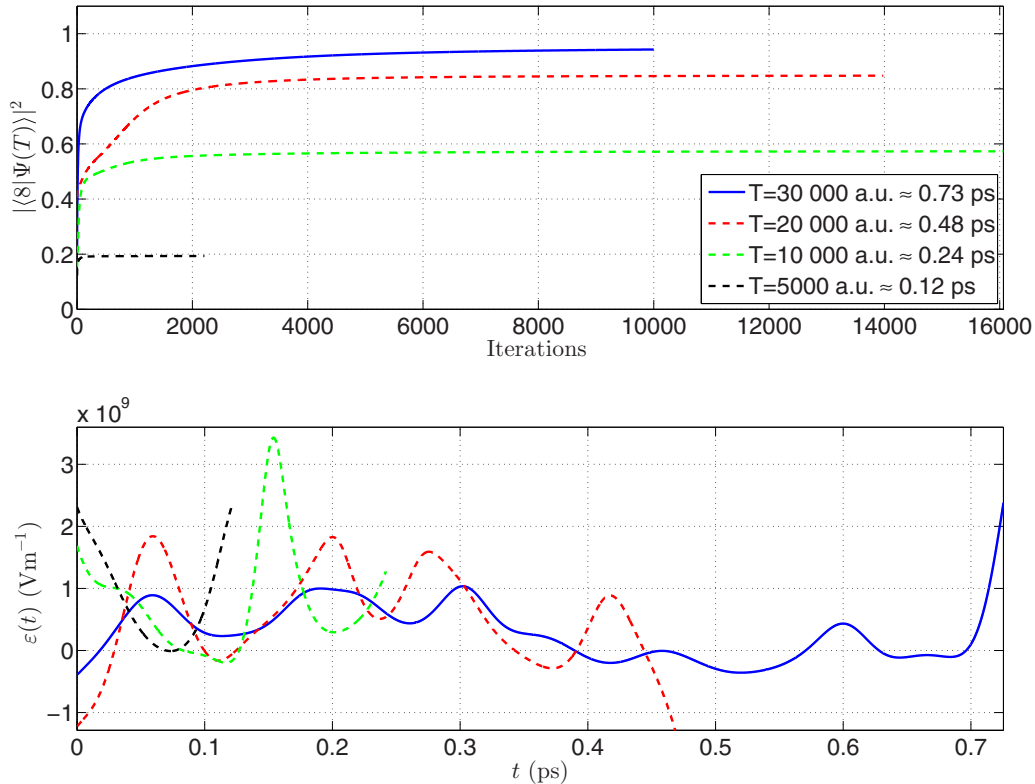
FIG. 7. (Color online) Upper panel: Transition probability as a function of iterations for the transition $|1\rangle \rightarrow |8\rangle$ (see Fig. 1). The dashed lines show the transition probabilities for optimal pulses of different durations (see the legend). The lines terminate at the number of iterations where the criteria of Eq. (36) is fulfilled. Lower panel: Optimized electric field $\varepsilon(t)$ obtained for pulses of different durations T. The number of iterations needed for a convergent solution vary with T, as seen in the upper panel. Key parameters: $\Delta t = 0.005$, $\epsilon_0 = 0.001$, $\alpha = 1$, all expressed in atomic units.

B. Dipole forbidden transition between rotational levels with Λ doubling and hyperfine structure

In this second example, we study the transition $|1\rangle \rightarrow |8\rangle$. Quantum numbers corresponding to states $|1\rangle$ and $|8\rangle$ are presented in Fig. 1. This particular transition is dipole forbidden. The two states $|1\rangle$ and $|8\rangle$ have the same parity eigenvalue, and $\Delta F = 2 \, (F = 1 \rightarrow F' = 3) \, (\Delta J = 1)$. The energy difference between the initial and final state is approximately 88 cm^{-1}.

From Figs. 1 and 2, two simple pathways from $|1\rangle$ to $|8\rangle$ can be identified,

$$|1\rangle \rightarrow |4\rangle \rightarrow |8\rangle \quad \text{(path 1)}, \tag{43}$$

$$|1\rangle \rightarrow |5\rangle \rightarrow |8\rangle \quad \text{(path 2)}. \tag{44}$$

The transition probabilities and the optimized electric fields are presented in Fig. 7 for $T = 5000, 10\,000, 20\,000$, and $30\,000$ a.u. Even though the transition $|1\rangle \rightarrow |8\rangle$ is dipole forbidden, a pulse that stimulates the transition is readily obtained. As expected, the occupation probability of the final state increases with the duration of the pulse T. However, compared to the transition studied in example A, the increase in the occupation probability as a function of T is more moderate.

The optimized electric fields as a function of time t are apparently similar to the ones obtained in example A. They consist of a large number of frequencies, are rather nonintuitive, and are strongly dependent on T. The field amplitudes are again seen to decrease with T, indicating a tendency towards "smoother" transitions. The penalty factor was set to $\alpha = 1$ as before.

In addition to the initial and final states, four states are found to be particularly important to achieve this dipole forbidden transition (Fig. 8). Of the two expected pathways identified in Eqs. (43) and (44), both are used. However, somewhat surprisingly, states $|18\rangle$ and $|19\rangle$ also join in. At the end of the pulse, the final state is populated from states $|19\rangle$ and $|4\rangle$. However, initially state $|5\rangle$ is heavily occupied due to the large dipole matrix element $\langle 1|\hat{d}|5\rangle = -0.27$ a.u. This occupation is then transferred to the final state ($\langle 5|\hat{d}|8\rangle = -0.054$ a.u.) together with state $|18\rangle$ ($\langle 5|\hat{d}|18\rangle = -0.30$ a.u.), and also back to the initial state, i.e., the local maximum in the initial-state population at about $t = 0.9 \times 10^4$ a.u. However, the transition probability from state $|5\rangle$ to the final state $|8\rangle$ is rather small, and the system at an early stage "decides" that there is a more efficient way to reach the goal, i.e., by invoking the less probable transition $|1\rangle \rightarrow |4\rangle$ ($\langle 1|\hat{d}|4\rangle = 0.13$ a.u.), which at later times leads to a large population of state $|4\rangle$. Then, finally, the rather strong transition $|4\rangle \rightarrow |8\rangle$ ($\langle 4|\hat{d}|8\rangle = 0.27$ a.u.) leads to a transition probability to the final state which is close to unity.

The quantity $|J_2|$ [cf. Eq. (1)] is included to control or minimize the total power conveyed by the external field during the pulse length. From Figs. 7 and 9, we notice that the
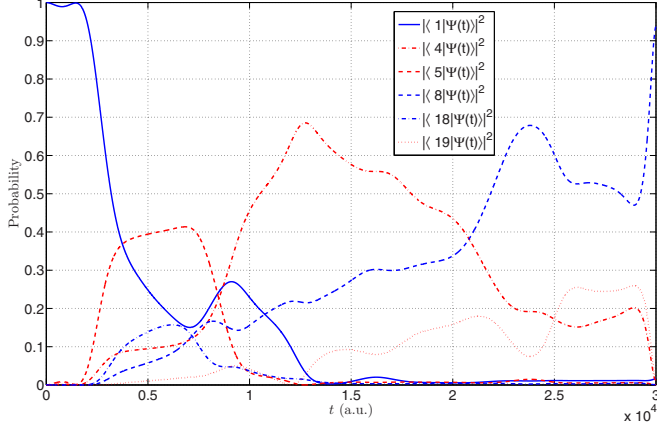
FIG. 8. (Color online) Occupation probabilities as a function of t for states that achieve an occupation probability larger than 0.05. Red (blue) is used to identify states with parity eigenvalue $+1$ (-1). These results were obtained with an optimized electric field of duration $T = 30\,000$ a.u.

longest pulse duration considered, i.e., $T = 30\,000$ a.u., yields a transition probability close to unity, as well as a small value of the applied power, and a smooth variation of the electric field. Thus, as found for example A, at some rather long duration T, the transition has the typical characteristics of an adiabatic process.

The duration of the pulses is less than 1 ps, and the bandwidth of the pulses may therefore cover several rotational states. Hence, the frequencies of the field $\varepsilon(t)$ could not be properly resolved in a fast Fourier transform (FFT) analysis.
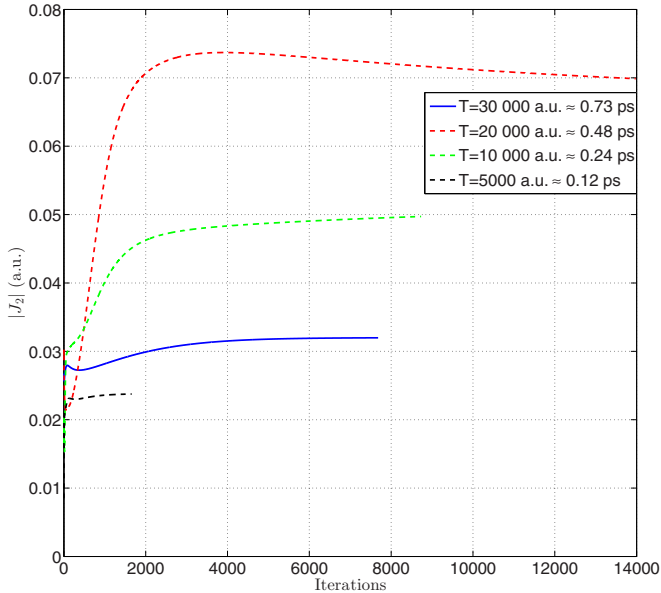

FIG. 9. (Color online) The quantity $|J_2|$ [see Eq. (42)] as a function of the number of iterations for example B. The iterations for the various values of T are terminated when the criteria of Eq. (36) are fulfilled.

VII. CONCLUDING REMARKS

The objective of the present work was twofold. We wanted to demonstrate how optimal control theory could be applied to a real diatomic molecule with both fine and hyperfine structure, and to present numerical examples. In conclusion, we have made a detailed study of a dipole allowed and a dipole forbidden transition between hyperfine states in OH. In both examples, the optimal pulses computed take the system from the initial state to the final state along complicated and unexpected pathways. Highly excited states contribute in the process, underlining the importance of using a complete set of spectroscopic constants to generate a large multitude of accurate energy levels.

Zhu *et al.* [11] reported that their iteration scheme converges to 80% of the final value in the first few iteration steps. However, Zhu *et al.* studied transitions between vibrational states and could achieve faster convergence because the pulse bandwidth did not cover several vibrational states. The optimal pulses in that work consisted of frequencies centered around the resonance frequencies. They induced transitions that were closer to the corresponding resonant transitions, compared with the optimal pulses in the present work. The truncation of the series representing $e^{i\hat{d}\varepsilon(t)\Delta t}$ in Eq. (21) may influence the convergence properties. We did, however, try to include the second-order term in Δt without any improvement. Werschnik and Gross [10] also pointed out that monotonic convergence could be proven analytically only when an infinitely accurate solution of the Schrödinger equation was assumed.

In practice, the solution of the Schrödinger equation for a diatomic molecule has to be based on a finite basis set. Furthermore, a finite set of molecular eigenstates has to be accepted in Eq. (23), which describes the action of the dipole moment operator on a molecular eigenstate. Thus, the truncation of the series expansion in Eq. (23), as well as other finite basis set effects, may affect the convergence properties of the present algorithm.

A few additional transitions were also studied as a part of the present work. Transitions between vibrational levels of the $X^2\Pi$ electronic state were considered. It proved difficult to obtain pulses that could achieve significant occupation probabilities of the final state when $\Delta v > 2$. Our investigation was, however, limited to pulses with a duration of $200\,000$ a.u. (i.e., $\simeq 5$ ps) or less. This limit stems from the computational cost involved in the calculations and does not represent a fundamental limit. A similar conclusion was drawn from some limited studies of transitions between the electronic states $X^2\Pi$ and $A^2\Sigma^+$.

APPENDIX A: DERIVATION OF EQUATION (33)

The molecular basis states used in the present work may be written as

$$|nv\Lambda\Sigma SI\Omega_I FM_F\Omega_F\rangle = |nv\Lambda\Sigma S\rangle|I\Omega_I\rangle|FM_F\Omega_F\rangle, \text{ (A1)}$$

with $\Omega_F \equiv \Lambda + \Sigma + \Omega_I$. The decomposition is in accordance with the Born-Oppenheimer approximation. M_F is the projection of the total spin angular momentum along a space fixed axis; the remaining quantum numbers in Eq. (A1) refer to the molecule fixed system which rotates with the nuclei (see

Sec. III). The orientation of the rotating system is described by the Eulerian angles (α, β, γ).

A rotating diatomic molecule is a symmetric top. The wave function of a symmetric top is given by an element of the rotational $\mathcal{D}$ matrix, and takes the form [23]

$$\psi_{FM_F\Omega_F}(\alpha,\beta,\gamma) = \sqrt{\frac{2F+1}{8\pi^2}}\mathcal{D}^F_{M_F\Omega_F}(\alpha,\beta,\gamma)^*, \quad \text{(A2)}$$

and

where Ω_F represents the quantum number corresponding to F_z, i.e., the component of the total molecular angular momentum along the molecule fixed symmetry axis. The $\mathcal{D}$ symbols are elements of the rotation matrices, and an extensive list of their properties and definitions can be found in Ref. [23]. In the present work, we need the following two properties:

$$\mathcal{D}^J_{Mm}(\alpha,\beta,\gamma)^* = (-1)^{M-m}\mathcal{D}^J_{-M-m}(\alpha,\beta,\gamma), \quad \text{(A3)}$$

$$\int \mathcal{D}^C_{cc'}(\alpha,\beta,\gamma)\mathcal{D}^A_{aa'}(\alpha,\beta,\gamma)\mathcal{D}^B_{bb'}(\alpha,\beta,\gamma)\sin\beta d\beta d\alpha d\gamma = 8\pi^2 \begin{pmatrix} A & B & C \\ a & b & c \end{pmatrix}\begin{pmatrix} A & B & C \\ a' & b' & c' \end{pmatrix}. \quad \text{(A4)}$$

The matrix elements that we need now take the form

$$\langle n'v'\Lambda'\Sigma SI\Omega_I F'M_F\Omega'_F|\hat{d}_z|nv\Lambda\Sigma SI\Omega_I FM_F\Omega_F\rangle$$

$$= \sum_{m=-1}^{1} \langle n'v'\Lambda'\Sigma S|d_m|nv\Lambda S\Sigma\rangle\langle I\Omega_I|I\Omega_I\rangle \langle F'M_F\Omega'_F|\mathcal{D}^{(1)}_{0m}(\alpha,\beta,\gamma)^*|FM_F\Omega_F\rangle. \quad \text{(A5)}$$

The rotational part of this matrix element can be worked out using Eqs. (A2) and (A3),

$$\langle F'M_F\Omega'_F|\mathcal{D}^{(1)}_{0m}(\alpha,\beta,\gamma)^*|FM_F\Omega_F\rangle$$

$$= \frac{\sqrt{(2F+1)(2F'+1)}}{8\pi^2}(-1)^{M_F-\Omega_F-m}\int \mathcal{D}^{F'}_{M_F\Omega'_F}(\alpha,\beta,\gamma)\mathcal{D}^{(1)}_{-0-m}(\alpha,\beta,\gamma)\mathcal{D}^F_{-M_F-\Omega_F}(\alpha,\beta,\gamma)\sin\beta d\beta d\alpha d\gamma. \quad \text{(A6)}$$

Finally, Eq. (A4) is used to obtain

$$\langle F'M_F\Omega'_F|\mathcal{D}^{(1)}_{0m}(\alpha,\beta,\gamma)^*|FM_F\Omega_F\rangle$$

$$= \sqrt{(2F+1)(2F'+1)}(-1)^{M_F-\Omega_F-m}\begin{pmatrix} 1 & F & F' \\ 0 & -M_F & M_F \end{pmatrix}\begin{pmatrix} 1 & F & F' \\ -m & -\Omega_F & \Omega_F \end{pmatrix}. \quad \text{(A7)}$$

Equation (33) follows from Eqs. (A5) and (A7). To arrive at the exact expression, one also needs to perform some cyclic permutations of the $3j$ symbols in Eq. (A7).

For more details, we refer to [21,22].

APPENDIX B: THE RELATIONSHIP BETWEEN THE BASIS STATES IN EQUATION (27) AND HUND'S COUPLING CASE (a_β)

In Hund's coupling case (a_β), the molecular basis states are of the form

$$|\psi_a\rangle = |nv\Lambda\Sigma SJIFM_F\rangle. \quad \text{(B1)}$$

The angular momentum $\vec{J}$ is coupled to the nuclear spin $\vec{I}$ to produce the grand total spin angular momentum $\vec{F} = \vec{J} + \vec{I}$. The molecular basis states $|\psi_a\rangle$ can be decoupled, factorizing out the nuclear spin part,

$$|\psi_a\rangle = \sum_{M_J,M_I} p_1\sqrt{2F+1}\begin{pmatrix} J & I & F \\ M_J & M_I & -M_F \end{pmatrix}|nv\Lambda S\Sigma\rangle|JM_J\Omega\rangle|IM_I\rangle. \quad \text{(B2)}$$

In Eq. (B2), $p_1 = (-1)^{J-I+M_F}$ is a phase factor.

The nuclear spin states $|IM_I\rangle$ are expanded in terms of the molecule-fixed spin states $|I\Omega_I\rangle$ as follows:

$$|IM_I\rangle = \sum_{\Omega_I} \mathcal{D}^I_{M_I\Omega_I}(\alpha,\beta,\gamma)^*|I\Omega_I\rangle, \quad \text{(B3)}$$

where the rotation matrices are used to rotate the nuclear spin states. The angles α, β, and γ are the Eulerian angles that describe the orientation of the rotating system.

We also need the rotational wave function of a diatomic molecule. The rotation matrices are eigenfunctions of the total angular momentum of a rigid body [23]. The nuclear spin part was decoupled from the molecular basis states in Eq. (B2). Hence, the ket $|JM_J\Omega\rangle$ now corresponds the rotational wave function in Eq. (A2) with F, M_F, and Ω_F replaced by J, M_J, and Ω (interested

readers are referred to [21,23]),

$$\psi_{JM_J\Omega}(\alpha,\beta,\gamma) = \sqrt{\frac{2J+1}{8\pi^2}}\mathcal{D}^J_{M_J\Omega}(\alpha,\beta,\gamma)^*. \tag{B4}$$

Inserting Eqs. (B3) and (B4) into Eq. (B2), we obtain

$$|\psi_a\rangle = \sum_{M_J,M_I} p_1\sqrt{\frac{2J+1}{8\pi^2}}\sqrt{2F+1}\begin{pmatrix} J & I & F \\ M_J & M_I & -M_F \end{pmatrix}\sum_{\Omega_I}\mathcal{D}^J_{M_J\Omega}(\alpha,\beta,\gamma)^*\mathcal{D}^I_{M_I\Omega_I}(\alpha,\beta,\gamma)^*|nv\Lambda\Sigma S\rangle|I\Omega_I\rangle. \tag{B5}$$

To recouple the right-hand side, we need the product of the two elements of the different rotation matrices. The necessary properties of the rotation matrices can be found in Ref. [23] and are reproduced here for convenience,

$$\mathcal{D}^J_{M_J\Omega}(\alpha,\beta,\gamma)^*\mathcal{D}^I_{M_I\Omega_I}(\alpha,\beta,\gamma)^* = \sum_{F'}(-1)^{M_F-\Omega_F}(2F'+1)\begin{pmatrix} J & I & F' \\ -M_J & -M_I & M_F \end{pmatrix}\begin{pmatrix} J & I & F' \\ -\Omega & -\Omega_I & \Omega_F \end{pmatrix}\mathcal{D}^{F'}_{M_F\Omega_F}(\alpha,\beta,\gamma)^*. \tag{B6}$$

This result is used to couple the two rotational matrices in Eq. (B5):

$$|\psi_a\rangle = \sum_{M_J,M_I} p_2\sqrt{\frac{2J+1}{8\pi^2}}\sqrt{2F+1}\begin{pmatrix} J & I & F \\ M_J & M_I & -M_F \end{pmatrix}\sum_{F',\Omega_I}(2F'+1)\begin{pmatrix} J & I & F' \\ -M_J & -M_I & M_F \end{pmatrix}$$

$$\times \begin{pmatrix} J & I & F' \\ -\Omega & -\Omega_I & \Omega_F \end{pmatrix}\mathcal{D}^{F'}_{M_F\Omega_F}(\alpha,\beta,\gamma)^*|nv\Lambda\Sigma S\rangle|I\Omega_I\rangle. \tag{B7}$$

The new phase factor $p_2 = p_1 \cdot (-1)^{M_F-\Omega_F} = (-1)^{J-I+2M_F-\Omega_F}$. The rather lengthy expression above is simplified by the orthogonality relation of the two $3j$ symbols that involve M_J, M_I, and M_F,

$$|\psi_a\rangle = p_2\sqrt{\frac{2J+1}{8\pi^2}}\sqrt{2F+1}\sum_{F',\Omega_I}(-1)^{J+I+F'}\begin{pmatrix} J & I & F' \\ -\Omega & -\Omega_I & \Omega_F \end{pmatrix}\mathcal{D}^{F'}_{M'_F\Omega_F}(\alpha,\beta,\gamma)^*\delta_{FF'}|nv\Lambda\Sigma S\rangle|I\Omega_I\rangle. \tag{B8}$$

The additional phase factor $(-1)^{J+I+F}$ comes from a necessary sign change $(-M_J \to M_J, -M_I \to M_I, M_F \to -M_F)$ in one of the $3j$ symbols before the orthogonality relation can be used. Equation (B8) can be further simplified by introducing the states $|FM_F\Omega_F\rangle$, in analogy with Eqs. (B4) and (A2),

$$|\psi_a\rangle = p_3\sqrt{2J+1}\sum_{\Omega_I}\begin{pmatrix} J & I & F \\ -\Omega & -\Omega_I & \Omega_F \end{pmatrix}|nv\Lambda\Sigma S\rangle|I\Omega_I\rangle|FM_F\Omega_F\rangle. \tag{B9}$$

The new phase factor $p_3 = p_2 \cdot (-1)^{J+I+F} = (-1)^{2J+2M_F+F-\Omega_F}$. The inverted relation is obtained by multiplying both sides of Eq. (B9) by a $3j$ symbol, and summing over J and Ω,

$$\sum_{J,\Omega} p\sqrt{2J+1}\begin{pmatrix} J & I & F \\ -\Omega & -\Omega'_I & \Omega'_F \end{pmatrix}|\psi_a\rangle$$

$$= \sum_{\Omega_I}\sum_{J,\Omega}(2J+1)\begin{pmatrix} J & I & F \\ -\Omega & -\Omega'_I & \Omega'_F \end{pmatrix}\begin{pmatrix} J & I & F \\ -\Omega & -\Omega_I & \Omega_F \end{pmatrix}|nv\Lambda\Sigma S\rangle|I\Omega_I\rangle|FM_F\Omega_F\rangle. \tag{B10}$$

Finally it follows from the orthogonality relation obeyed by the $3j$ symbols that

$$|nv\Lambda\Sigma SI\Omega_I FM_F\Omega_F\rangle = \sum_{J,\Omega} p\sqrt{2J+1}\begin{pmatrix} J & I & F \\ -\Omega & -\Omega_I & \Omega_F \end{pmatrix}|\psi_a\rangle. \tag{B11}$$

The summation over Ω is redundant when Λ and Σ are quantized and $\Omega = \Lambda + \Sigma$. The phase factor $p = (-1)^{\Omega_F-2J-2M_F-F}$. For OH, the quantum number M_F is always an integer and $(-1)^{2M_F} = 1$. However, in general, F and M_F can take half-integer values.

Equation (B11) makes it clear why J is not a good quantum number in the basis set. Equation (B11) also gives the basis states in terms of the Hund's coupling case (a_β) basis states. For more details, we refer the reader to [21,22].

---

[1] C. M. Tesch and R. de Vivie-Riedle, Phys. Rev. Lett. **89**, 157901 (2002).

[2] K. Rojan, D. M. Reich, I. Dotsenko, J.-M. Raimond, C. P. Koch, and G. Morigi, Phys. Rev. A **90**, 023824 (2014).

[3] G. De Chiara, T. Calarco, M. Anderlini, S. Montangero, P. J. Lee, B. L. Brown, W. D. Phillips, and J. V. Porto, Phys. Rev. A **77**, 052333 (2008).

[4] T. Caneva, M. Murphy, T. Calarco, R. Fazio, S. Montangero, V. Giovannetti, and G. E. Santoro, Phys. Rev. Lett. **103**, 240501 (2009).

[5] C. J. Bardeen, V. V. Yakovlev, K. R. Wilson, S. D. Carpenter, P. M. Weber, and W. S. Warren, Chem. Phys. Lett. **280**, 151 (1997).

[6] T. Brixner, N. H. Damrauer, P. Niklaus, and G. Gerber, Nature (London) **414**, 57 (2001).

[7] A. Assion, T. Baumert, M. Bergt, T. Brixner, B. Kiefer, V. Seyfried, M. Strehle, and G. Gerber, Science **282**, 919 (1998).

[8] J. L. Herek, W. Wohlleben, R. J. Cogdell, D. Zeidler, and M. Motzkus, Nature (London) **417**, 533 (2002).

[9] R. S. Judson and H. Rabitz, Phys. Rev. Lett. **68**, 1500 (1992).

[10] J. Werschnik and E. K. U. Gross, J. Phys. B **40**, R175 (2007).

[11] W. Zhu, J. Botina, and H. Rabitz, J. Chem. Phys. **108**, 1953 (1998).

[12] W. Zhu and H. Rabitz, J. Chem. Phys. **109**, 385 (1998).

[13] Y. Maday and G. Turinici, J. Chem. Phys. **118**, 8191 (2003).

[14] C. P. Koch, J. P. Palao, R. Kosloff, and F. Masnou-Seeuws, Phys. Rev. A **70**, 013402 (2004).

[15] G. Strang, SIAM J. Numer. Anal. **5**, 506 (1968).

[16] J. Brown and A. Carrington, *Rotational Spectroscopy of Diatomic Molecules*, Cambridge Molecular Science (Cambridge University Press, Cambridge, 2003), p. 232.

[17] G. Herzberg, *Spectra of Diatomic Molecules*, *Molecular Spectra and Molecular Structure* (Van Nostrand, New York, 1950).

[18] J. T. Hougen, NBS Monograph **115**, 1 (1970).

[19] R. Zare, A. Schmeltekopf, W. Harrop, and D. Albritton, J. Mol. Spectrosc. **46**, 37 (1973).

[20] A. R. Edmonds, *Angular Momentum in Quantum Mechanics* (Princeton University Press, Princeton, NJ, 1974).

[21] L. Veseth, http://folk.uio.no/leifve/Rotasjonsgruppen.pdf (unpublished).

[22] L. Veseth, http://folk.uio.no/leifve/Molspec.pdf (unpublished).

[23] D. M. Brink and G. R. Satchler, *Angular Momentum* (Oxford University Press, New York, 1993).

[24] M. Lysebo and L. Veseth, Phys. Rev. A **83**, 033407 (2011).

[25] W. J. Stevens, G. Das, A. C. Wahl, M. Krauss, and D. Neumann, J. Chem. Phys. **61**, 3686 (1974).

[26] L. Veseth, J. Mol. Spectrosc. **59**, 51 (1976).

[27] L. Veseth, J. Mol. Spectrosc. **63**, 180 (1976).

[28] R. A. Beaudet and R. L. Poynter, J. Phys. Chem. Ref. Data **7**, 311 (1978).

[29] R. A. Frosch and H. M. Foley, Phys. Rev. **88**, 1337 (1952).

[30] G. C. Dousmanis, Phys. Rev. **97**, 967 (1955).

[31] P. Kristiansen and L. Veseth, J. Chem. Phys. **84**, 2711 (1986).

[32] J. Coxon and S. Foster, J. Mol. Spectrosc. **91**, 243 (1982).

[33] M. Demiralp and H. Rabitz, Phys. Rev. A **47**, 809 (1993).